POLITECNICO DI TORINO
Repository ISTITUZIONALE

Exploring Semiconductor Qubits: Simulation of a Four Quantum Dot Silicon Device

Original
Exploring Semiconductor Qubits: Simulation of a Four Quantum Dot Silicon Device / Pedicini, G., Tudisco, A., Cignoni, M., Graziano, M., Piccinini, G., Riente, F.. - In: QUANTUM SCIENCE AND TECHNOLOGY. - ISSN 2058-9565. - 10:(2025). [10.1088/2058-9565/adf6d1]

Availability:
This version is available at: 11583/3002298 since: 2025-08-02T05:54:19Z

Publisher:
IOP Publishing

Published
DOI:10.1088/2058-9565/adf6d1

Terms of use:

This article is made available under terms and conditions as specified in the corresponding bibliographic description in the repository

Publisher copyright

(Article begins on next page)

18 November 2026

Quantum Science and Technology

Celebrating the 10th anniversary of Quantum Science and Technology
INTERNATIONAL YEAR OF Quantum Science and Technology
PURPOSE-LED PUBLISHING™

PAPER • **OPEN ACCESS**

Exploring semiconductor qubits: simulation of a four quantum dot silicon device

To cite this article: Giovanni Pedicini *et al* 2025 *Quantum Sci. Technol.* **10** 045012

View the article online for updates and enhancements.

You may also like

- Complexity of Gaussian quantum optics with a limited number of non-linearities
Michael G Jabbour and Leonardo Novo
- A general approach to quantum integration of cross sections in high-energy physics
Ifan Williams and Mathieu Pellen
- State-agnostic approach to certifying electron–photon entanglement in electron microscopy
Phila Rembold, Santiago Beltrán-Romero, Alexander Preimesberger et al.

This content was downloaded from IP address 130.192.232.211 on 02/09/2025 at 10:17

IOP Publishing Quantum Sci. Technol. 10 (2025) 045012 https://doi.org/10.1088/2058-9565/adf6d1

Quantum Science and Technology



OPEN ACCESS

RECEIVED
18 March 2025

REVISED
3 July 2025

ACCEPTED FOR PUBLICATION
1 August 2025

PUBLISHED
12 August 2025

Original Content from this work may be used under the terms of the Creative Commons Attribution 4.0 licence.

Any further distribution of this work must maintain attribution to the author(s) and the title of the work, journal citation and DOI.



PAPER

Exploring semiconductor qubits: simulation of a four quantum dot silicon device

Giovanni Pedicini[1], Antonio Tudisco[2,*], Mario Cignoni[3], Mariagrazia Graziano[4], Gianluca Piccinini[2] and Fabrizio Riente[2]

[1] Univ. Grenoble Alpes, CEA, Grenoble INP, IRIG–Pheliqs, 38000 Grenoble, France
[2] Department of Electronics and Telecommunications, Politecnico di Torino,Corso Castelfidardo 39, 10129 Torino, Italy
[3] University of Twente, Drienerlolaan 5, 7522 NB Enschede, The Netherlands
[4] Department of Applied Science and Technology, Politecnico di Torino, Corso Duca degli Abruzzi 24, 10129 Torino, Italy
* Author to whom any correspondence should be addressed.

E-mail: antonio.tudisco@polito.it, giovanni.pedicini@cea.fr, m.cignoni@utwente.nl, mariagrazia.graziano@polito.it, gianluca.piccinini@polito.it and fabrizio.riente@polito.it

Keywords: quantum dots, semiconductor qubits, quantum device, quantum simulation

Abstract

Quantum computing represents a revolutionary computational paradigm with the potential to overcome the limitations of classical computers. Among the various approaches under investigation, semiconductor-based solutions stand out as promising candidates for qubit implementation. This work explores a four-quantum dot SiGe heterostructure. The above structure has been analyzed using the low-level finite element method-based simulator quantum technology computer-aided design (QTCAD) to derive essential physical parameters critical for implementing electron spin qubits. Even though QTCAD may not be as accurate as real experiments, it nonetheless provides important insights into the device behavior. The aim is to use these simulations to effectively analyze the device's response to changes in structural parameters and determine whether it is feasible for real-world applications. As a result, changes to the structure can be made by simply modifying the simulation code, avoiding the need for repetitive and expensive lithographic processes. Notably, this is the first time a four-quantum-dot system has been analyzed using QTCAD. Specifically, the study involves solving the non-linear Poisson equation as well as single and multi particle Schrödinger equations. Additionally, a transport analysis is performed, yielding Coulomb peaks, Coulomb diamonds, and charge stability diagrams. Finally, an approximation of the tunneling coefficient and the exchange interaction energy between the different dot pairs is computed. The results provide a foundation for the design of advanced logic circuits able to execute multiple quantum logic gates. By leveraging the precise control over quantum dot configuration, it becomes possible to customize the interactions between quantum states for specific computational purposes. This approach enables the realization of complex architectures where individual quantum dots act as qubits or nodes in a quantum network. The ability to tune gate voltages and control inter-dot couplings allows for the implementation of complex quantum logic gates.

1. Introduction

The previous decade witnessed a continuous advancement in quantum devices constructed from semiconductor materials. Indeed, this trend arose from the significant limitations encountered by classical electronics across numerous applications. Quantum electronics, especially quantum computing, emerged as a promising solution for achieving functionalities that are not possible with classical electronics. Various technologies have been proposed to enhance the development of quantum technologies, with semiconductor quantum technologies being among the most promising. It is now possible to achieve very high fidelity quantum gate using semiconductor qubits [1] since semiconductor devices allow for the implementation of

© 2025 The Author(s). Published by IOP Publishing Ltd

qubits with extended coherence time [2]. After decades of advancement, it became evident that silicon is one of the optimal materials for next-generation devices leveraging quantum properties of charge and spin. In this article, the emphasis is placed on quantum dots with confinement in all three dimensions, which, due to their flexibility, scalability, and compatibility with CMOS integration techniques, are among the most promising options for qubits. Nevertheless dopants [3] and optically addressable quantum defects [4] provide alternative approaches in semiconductors.

Quantum dot electron qubits can be encoded, considering the confinement of the electrons, using different methodologies: the spin-$\frac{1}{2}$ qubit, where the information is stored on the hyperfine Zeeman levels, in particular the zero state is $|\downarrow\rangle$ and the one state is $|\uparrow\rangle$ [2], the charge qubit that exploits the charge of a physical system to represent quantum information [5], the singlet–triplet (ST) qubit that relies on the singlet and triplet states of two electrons confined within a double quantum dot system and the hybrid qubit, which stands out for its unique encoding scheme, leveraging both electron positions and spins. This study focuses on the physical properties of a four quantum dots SiGe/Si/SiGe heterostructure, used to encode spin-$\frac{1}{2}$ qubit, described in [6].

A dedicated software tool called quantum technology computer-aided design (QTCAD) [7], by Nanoacademic Technologies, is used to examine the heterostructure. The purpose of the article is to analyze carrier dynamics and transport properties inside a silicon heterostructure based on four quantum dots similar to studies presented in the literature, for instance [8]. However, unlike those approaches where the confinement potential is defined analytically, this work begins by solving the non-linear Poisson equation, followed by the single-particle and multi-particle Schrödinger equations, before performing the transport analysis. The study builds upon earlier publications that employed QTCAD to simulate semiconductor quantum dot heterostructures, including [9]. The tunneling coupling approximation and the exchange interaction energy are calculated to quantify the coupling between different pairs of quantum dots. Moreover, the simulation of Coulomb diamonds, Coulomb peaks, and charge stability diagrams offers a summary of the heterostructure transport characteristics.

2. Theoretical foundation

2.1. Non-linear Poisson equation

To simulate the proposed heterostructure, the methodological workflow prescribed by QTCAD is followed. The initial phase involves the precise definition of the computational mesh, a critical step achieved through the utilization of a third-party open-source software tool, GMSH [10], which facilitates the generation of geometry-specific meshing parameters. As described in [7], QTCAD is a finite element method (FEM) solver for quantum devices, able to extract key physical properties. The assignment of materials and boundary conditions to distinct regions of the structure enables QTCAD to solve the non-linear Poisson equation, a necessary step for obtaining some device characteristics, such as the conduction band edge and electrostatic profile, as detailed in [11].

2.2. Schrödinger equation

The program employs the envelope-function approximation (EFA) to address the time-independent single particle Schrödinger equation in domains where classical physics is inadequate [12], allowing the computation of bound states, their probability density distributions, and associated energy levels [13]. The validity of EFA is based on the separation between the slow-varying confinement potential imposed by the nanostructure and the rapidly oscillating atomistic potential, ensuring that the second can be averaged out.

For electrons, QTCAD utilizes the effective-mass approximation under the assumption of a single quadratic band, providing a simplified yet precise treatment of quantum confinement effects.

For systems containing multiple quantum dots, a multi particle simulation is necessary to accurately reflect quantum-mechanical interactions between confined particles [14], as single particle solvers can only provide approximations. QTCAD addresses this limitation through its many-body solver, which employs the exact-diagonalization method, enabling a precise representation of exchange and correlation effects [15, 16]. By incorporating these effects, QTCAD provides a more accurate and comprehensive framework for modeling many-body interactions in quantum dot systems. Although many-body analyses can be time-consuming, the Fermi–Hubbard model provides a simple but effective method for capturing the complex physics of a multi electron system, such as four quantum dots [17]:

$$H_{\mathrm{D}} \approx \sum_{i\sigma} \epsilon_{i\sigma} n_{i\sigma} + \sum_{i} \frac{U_i}{2} n_i (n_i - 1) + \frac{1}{2} \sum_{j, j \neq i} V_{ij} n_i n_j, \tag{1}$$

where the particle operators $n_i = \sum_\sigma n_{i\sigma}, n_{i\sigma} = c^\dagger_{i\sigma} c_{i\sigma}$ and the Coulomb interaction energies U_i and V_i are introduced. The main advantage of this approximation with respect the exact diagonalization method is that the number of Coulomb integrals to evaluate for n_{states} single particle states scales like $\mathcal{O}(n^2_{\text{states}})$ instead of $\mathcal{O}(n^4_{\text{states}})$ when overlap terms are included, as discussed in [18].

2.3. Transport in Coulomb blockade regime

Accurate modeling and description of quantum transport processes is possible after the many-body solver is configured correctly within the QTCAD framework [19]. This method considers the device as a junction where quantum dots are connected to source and drain leads, with supplementary gates regulating potential confinement, and carrier motion occurs via tunneling between distinct energy levels. Within QTCAD's transport solver, the many-body characterization of the device is obtained by adding the coupling between the quantum region and the leads, that is generated from tunneling events:

$$H = \sum_{i\sigma} \epsilon_{i\sigma} \hat{c}^\dagger_{i\sigma} c_{i\sigma} + \frac{1}{2} \sum_{ijkl,\sigma\sigma'} V_{ijlk} \hat{c}^\dagger_{i\sigma} \hat{c}^\dagger_{j\sigma'} \hat{c}_{k\sigma} \hat{c}_{l\sigma} + \sum_{\mathbf{k}L} \epsilon_{\mathbf{k}L} c^\dagger_{\mathbf{k}L} c_{\mathbf{k}L} + \sum_{\mathbf{k}L,i\sigma} \left(t^*_{\mathbf{k}L,i\sigma} c^\dagger_{\mathbf{k}L} c_{i\sigma} + H.c. \right) \tag{2}$$

where the first term corresponds to the kinetic energy, the second one describes the coulomb electron-electron interaction, the third term is the free Hamiltonian of source and drain with $\epsilon_{\mathbf{k}L}$ the energy of a lead $L \in [D, S]$ eigenstate with wave vector $\mathbf{k}$. The last term of the equation describes the tunneling between the device and the leads, with $t_{\mathbf{k}L,i\sigma}$ the tunneling matrix element between the single electron eigenstates $(i\sigma)$ of the quantum region and the eigenstates $\mathbf{k}$ of the lead L. In the QTCAD transport regime, the many-body device Hamiltonian is solved using the exact diagonalization method and the interactions between the source, the drain and the dot, modeled as a weak perturbation. Finally, the master equation [19] governs the dynamics of charge flow, and enables the calculation of transport features such as Coulomb peaks, Coulomb diamonds, and charge stability diagrams, which are crucial for analyzing the single electron transport regime.

2.4. The non-equilibrium Green's function (NEGF)

The NEGF formalism is a powerful tool for modeling non-equilibrium quantum statistical phenomena, making it capable of simulating both classical and quantum transport processes in devices with arbitrary geometry, material composition, temperature conditions, and external bias voltages [20, 21]. However, one significant shortcoming of the NEGF approach used in QTCAD, compared to more thorough many-body formalisms is its omission of electron-electron (or hole-hole) interactions. As a result, the NEGF formalism fails to capture Coulomb blockade phenomena, which result from strong interactions between charged particles in confined regions and are required for accurately describing transport in systems where electron interactions have a significant influence on device behavior. Furthermore, while the NEGF formalism explicitly accounts for the influence of the source and drain on the center region, but it neglects to consider the effect of the central region on the source and drain. For example, the NEGF formalism cannot account for Coulomb repulsion or attraction caused by a considerable charge accumulation in the core region of the source and drain next to it. This limitation arises from an underlying assumption of the NEGF formalism: the source and the drain are treated as thermal reservoirs with uniform and unchanging physical properties. For the assumption to hold, buffer regions near the source/drain boundaries must be included in the central region, and the electric potential in the buffer regions should gradually plateau to a constant value near the source/drain interfaces, as they serve as transitional areas between the center region and the source/drain.

3. Implementation

3.1. Device structure

The device analyzed using QTCAD is a SiGe heterostructure four-quantum-dot used to implement electron spin qubits. The heterostructure, as described in [6], begins with a 2.5 μm strained relaxed $Si_{0.7}Ge_{0.3}$ layer, which is reduced to 30 nm in the simulation for computational efficiency. On top of the $Si_{0.7}Ge_{0.3}$ layer is a 9 nm isotropically enriched ^{28}Si quantum layer. This quantum layer is separated from the 1 nm Si cap by another 30 nm relaxed $Si_{0.7}Ge_{0.3}$ layer, which completes the heterostructure. However, in the experimental setup, the Si cap oxidizes before the atomic layer deposition of the top oxide (Al_2O_3), thus it is not considered in the simulation. Instead, only 10 nm of Al_2O_3 is used to separate the gate stack from the heterostructure.

The device comprises a three-layer gate metal stack: Y-gates, dot plunger gates and reservoir gates, and barrier gates, as depicted in figure 1. The three gate layers are made of Ti:Pd, but to simplify the structure in

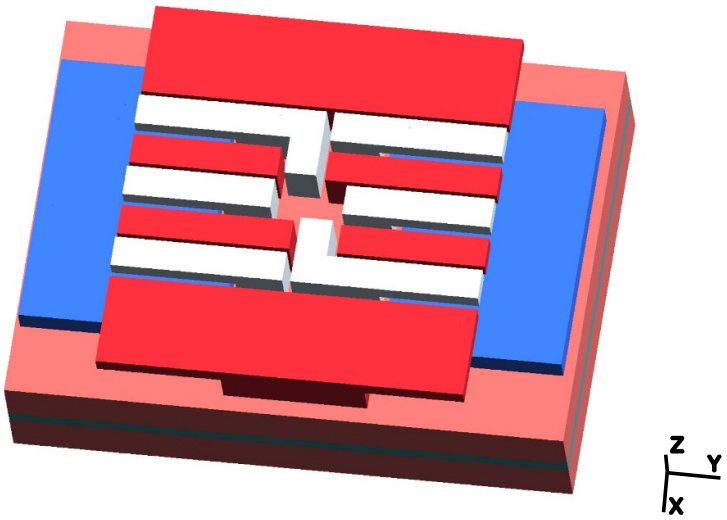


Figure 1. SiGe four quantum dot heterostructure obtained with GMSH [10]. The graphic depicts the structure of gate layers. The blue layer confinement gates create an active region and prevent the formation of false dots. The second layer consists of reservoir gates and the four dot plunger gates (in red). The third (white) layer is where barrier gates are constructed.

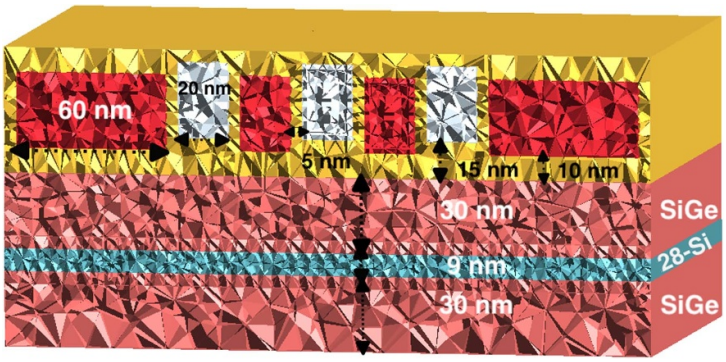


Figure 2. SiGe four quantum dot heterostructure obtained with GMSH [10]. The figure reports a cut of the structure along a plane perpendicular to the XY plane in the quantum region.

the QTCAD simulation, the metal gates are represented by boundary conditions defined at the interface between the oxide structure and the gate region. Each metal layer is separated from the underlying one by 5 nm of oxide. The height of the Y gates is 15 nm, while their width varies along the $\hat{x}$ direction. Specifically, the Y gate in the upper region has a width of 127.5 nm from $x = 40$ nm to 115 nm, and then it is 112.5 nm wide, whereas in the lower region, the Y gates are 112.5 nm wide from $x = 40$ nm to 145 nm, and then 127.5 nm wide.

The extension of the dot plungers and barriers over the quantum region is 20 nm along the $\hat{x}$ direction, 30 nm along the $\hat{y}$ direction, and 30 nm along the $\hat{z}$ direction, as shown in figure 2. However, the right upper barrier and the left lower barrier must separate the dot from the reservoir gates and the two dots along the $\hat{y}$ direction. Therefore, in the simulation, as described in figure 1, these two barrier gates have an L shape, with extensions of 55 nm along the $\hat{y}$ direction and 45 nm along the $\hat{x}$ direction. The reservoir gates have the same dimensions as the dot plungers along the $\hat{z}$ and $\hat{y}$ directions and 60 nm along the $\hat{x}$ direction, even though they are not aligned as in the two previous cases but rigidly shifted to accommodate the Y gates. Along the $\hat{x}$ direction, the barriers and plungers are separated by 5 nm of oxide. The Y gates are separated from the barriers and plungers by 5 nm of oxide.

Finally, there are four ohmic contacts at the four corners of the structure, each with a volume of $40 \times 60 \times 44\,\text{nm}^3$. Therefore, they include the top $Si_{0.7}Ge_{0.3}$, the ^{28}Si quantum layer, and 5 nm of the $Si_{0.7}Ge_{0.3}$ below the quantum layer. These ohmic regions are n^+ doped, with a dopant concentration of $5 \times 10^{18}\,\text{cm}^{-3}$.

3.2. Simulation parameters

For this simulation, the temperature is fixed at 15 mK, and the dopant concentration is set to $N_D = 1 \times 10^{18}\,cm^{-3}$, with complete ionization assumed. Additionally, the metal workfunction is considered to be:

$$\phi_m = \chi_{Si_{0.7}Ge_{0.3}} + \frac{E_{g\text{-}Si_{0.7}Ge_{0.3}}}{2} \tag{3}$$

where $\chi_{Si_{0.7}Ge_{0.3}}$ and $E_{g\text{-}Si_{0.7}Ge_{0.3}}$ are the electron affinity and the band gap energy of $Si_{0.7}Ge_{0.3}$. The mesh derived via GMSH has a resolution of 4 nm in the lowest $Si_{0.7}Ge_{0.3}$ layer, 2 nm above and below the quantum layer, 1 nm inside the quantum layer, and 4 to 2 nm in the upper three gate layers. QTCAD cannot compute the strain from material and geometry definitions, thus, as demonstrated in [9], a potential of −0.146 V is provided to the Si quantum layer to align the conduction band minimum of $Si_{0.7}Ge_{0.3}$ with that of ^{28}Si.

3.3. Non-linear Poisson equation

The non-linear Poisson equation is solved iteratively, with mesh refinement at each iteration until the error reaches the threshold of 1×10^{-7}. Once convergence is achieved, the potential distribution and classical electron population across the device is obtained.

3.4. Single particle Schrödinger equation

Classical physics is inadequate for analyzing the electron population within the quantum layer. For this reason, a quantum mechanics approach is employed by solving the single particle Schrödinger equation. Specifically, the Schrödinger equation is solved in the quantum region, which has the following dimensions:

- along the $\hat{x}$ axis, from $x = 70$ nm to 190 nm
- along the $\hat{y}$ axis, from $y = 60$ nm to 290 nm
- along the $\hat{z}$ axis, from $z = 25$ nm to 44 nm.

In this case, the threshold error is set to 1×10^{-9}. From the solution of the single particle Schrödinger equation, five eigenstates and the corresponding eigenenergies are obtained, as this number is sufficient to obtain accurate eigenspectra for the first two states, which are the ones of interest. Finally, an approximation of the tunneling coupling between the dots is employed, as proposed in [22]:

$$t_0 \approx \frac{E_1 - E_0}{2} \tag{4}$$

where E_1 and E_0 are the first excited level energy and the ground state level energy respectively, with zero detuning.

3.5. Lever arm

The *lever arm*, a dimensionless coefficient that quantifies the ability of a gate to affect the electrochemical potential μ of a quantum dot, can be calculated once the Poisson and Schrödinger equations for the reference potential configuration have been solved. It specifically measures the extent to which changes in the gate voltage can tune the quantum dot's potential and, consequently, the electrochemical potential associated with it, which is critical for understanding quantum dot device control in experimental setups,

$$\mu = \mu_0 - e\alpha_G V_G \tag{5}$$

where $e > 0$ is the elementary charge and μ_0 is the dot's electro-chemical potential when $V_G = 0$. Taking into account that the electro-chemical potential is defined as [23]:

$$\mu = E_{tot}(N) - E_{tot}(N-1) \tag{6}$$

where $E_{tot}(N)$ is the total energy of the dot in N-electrons ground state, and considering the constant interaction model [24], the lever arm is defined as:

$$\alpha_G = -\frac{C_{0G}}{C_\Sigma} \tag{7}$$

The capacitance between the dot and the gate is represented by C_{0G} and the dot's self-capacitance is indicated by C_Σ.

Nevertheless, the lever arm can be explicitly computed by performing a linear fit of the response to changes in gate bias, without calculating the capacitances directly. Additionally, QTCAD has a module that automatically determines the lever arm by calculating the non-linear Poisson equation and the single particle Schrödinger equation for various bias values of V_G, while maintaining the other gate voltages constant. Finally, a linear fit of the different ground-state energies with respect to the gate voltage is calculated, where the slope is the lever arm coefficient.

3.6. Multi particle Schrödinger equation

Since the heterostructure is designed to implement electron spin qubits within quantum dots, the presence of more than one electron in the system must be considered. For this reason, a many body Schrödinger equation solver is used to analyze the interaction between the dots and to perform a transport analysis. Specifically, the exchange interaction energy between the different dot pairs is calculated using two different method, as defined in [2]. The first one, called perturbative kinetic method, is based on the Fermi Hubbard model approximation (section 2.2), which offers a practical approach for simplifying the evaluation of Coulomb integrals in the context of double quantum dot, when the off-diagonal terms of Coulomb matrix are negligible compared to diagonal terms. The Coulomb interactions between dots are neglected (no overlap terms), and instead the focus is on the kinetic exchange interaction, which arises from the combined action of the Pauli exclusion principle and tunneling between the quantum dots. For this reason, the exchange interaction energy can be computed through the tunneling coupling approximation of equation (4) and the on-site Coulomb interaction. In particular the equation used is:

$$J \approx \frac{2t_0^2}{U} \tag{8}$$

where U is the first element of the on-site Coulomb interaction of the Coulomb matrix, and t_0 is the tunneling coupling approximation.

Within the second method, as explained in section 2.2, the two-electron system is exactly diagonalized within a reduced single electron basis set. The latter provides the most comprehensive theoretical description but is also the most computationally expensive. The exchange interaction energy is then computed as the difference between the singlet and the three degenerate triplet states. A mesh characteristic length of 0.1 nm is defined to refine the mesh within the quantum dot region and achieve convergence for the exchange interaction energy, and a high number of states is necessary for proper convergence, otherwise, the ground state remains triple degenerate where the first state is the singlet state and the other two are triplet states. This suggests that the basis set is too small, so a convergence test to confirm that the exchange value stabilizes as the number of states increases is performed, and a steady value is found by employing a total of 30 states with a degeneracy factor of two. Physically, the exchange interaction energy measures the overlap between the wavefunctions of electrons in different dots, which can be tuned varying the barrier gates and t_0 control. When two dots are considered as two qubits, for instance, activating this interaction results in conditional shifts of their resonance frequencies, indicating that one qubit state is dependent upon the other [25].

3.7. Transport analysis

Transport analysis is fundamental for understanding how electrons move between the quantized energy levels of quantum dots, and this information is crucial for optimizing the performance of qubits based on quantum dots. In a multiple quantum dot scenario, solving the single particle Schrödinger equation alone is insufficient, so a comprehensive transport analysis of the structure is performed using the QTCAD many-body solver, which allows to compute Coulomb peaks, Coulomb diamonds, and charge stability diagrams.

3.7.1. Coulomb peaks

Coulomb peaks are a series of sharp peaks observed in the current of a quantum dot system as a function of plunger gate voltage. The spacing between two peaks corresponds to the energy required for the quantum dot to transition from a state with N electrons to a state with $N+1$ electrons. Since a 1D analysis is necessary to compute the Coulomb peaks, as discussed in [26], the structure must be reduced to a single dot. Accordingly to isolate the different dots, four specific gates voltages configurations are found.

The device is modeled as a junction, as detailed in section 2.3, where Coulomb peaks are obtained by computing the current flowing through the device, ensuring a non-negligible current, and the temperature is set to 1 K. The current plateau and the differential conductance peaks are broadened due to the Fermi–Dirac distribution [19], which describes the temperature dependence of the broadening. Regarding the tunneling dependence of the broadening, three approximations may be used in QTCAD. The first approach is to use

the featureless approximation, which models the transport regime as described in section 2.3, by assuming a constant value for the broadening function. As a result, this technique implies that the tunneling-dependent broadening function is virtually independent of both the source-drain bias range and the single particle basis state index. However, within these approximations, only the position and shape of peaks and plateaus associated with charge transitions can be predicted for the current and conductivity, while their absolute values cannot be accurately determined. The second method, known as the Wentzel–Kramers–Brillouin (WKB) approximation [27], provides more accurate quantitative predictions of current and conductivity in the sequential tunneling regime. It uses the master equation as in the previous case, but the tunneling-dependent broadening is no longer considered constant. Additionally, this method requires confinement in two directions within the contact regions. Specifically, since $\hat{x}$ is the transport direction in this analysis, the contacts may be confined along $\hat{y}$ and $\hat{z}$. However, this confinement is absent in this device, as the Y-gates, described in section 2, ensure confinement along the $\hat{y}$ direction within the plunger and barrier gate region but are not present at the source and drain contacts. To address this, a technique which includes tunneling broadening using the NEGF formalism is employed, by estimation the transmission coefficient and integrating it into the Laundauer–Buttiker equation, as done in [28].

As described in section 2.4, the NEGF formalism is restricted to the single electron regime. Therefore, current values are first obtained using the featureless approximation by sweeping the plunger gate voltage while fixing the source-drain voltage to a small value, and then the NEGF current is used to scale these. This means that peaks positions are determined using the featureless approximation, with the NEGF current corresponding to the current associated with the first Coulomb peak. Specifically, four states with a degeneracy of two are considered in the analysis, as this is the smallest number of states required to achieve convergence for the first two peaks, which are of primary interest since the structure is used to implement the spin qubit.

3.7.2. Coulomb diamonds

The Coulomb diamonds illustrate the relationship between differential conductance, source-drain voltage, and gate voltage, requiring a one-dimensional analysis as in section 3.7.1, with a non negligible current ensured by setting the temperature to 1 K. An additional approximation is exploited, where instead of calculating the full differential conductance, only the difference between the extreme current values at different potential configurations is considered, with the current values position are determined following the same methodology used for the Coulomb peaks, outlined in section 3.7.1. The only difference is that the current values, using the featureless approximation, are obtained by sweeping both the plunger gate voltage and the source-drain voltage.

3.7.3. Charge stability diagram

The charge stability diagram illustrates how the equilibrium electron occupancy changes varying the voltages applied to the plunger gates. As discussed in section 2.2, the Fermi–Hubbard model provides a practical approach to simplify the evaluation of Coulomb integrals in the context of double quantum dots, with four states with a degeneracy of two considered in the analysis. The charge stability diagram can be obtained using the sequential tunneling current, which typically requires long simulation times. A more efficient approach to quickly speed up this process is to consider as main quantity the total number of particles in the system instead of the sequential tunneling current. Indeed, changes in the total number of particles correspond to peaks in the particle addition spectrum, representing the energy needed to add an electron to the system, as defined by [17]:

$$\frac{\partial \langle N \rangle}{\partial \mu} = \frac{\langle N^2 \rangle - \langle N \rangle^2}{k_B T} \tag{9}$$

where k_B is the Boltzmann constant, T is the temperature, μ is the chemical potential (related to the plunger gate voltage), $\langle N \rangle$ is the average number of particles, $\langle N^2 \rangle$ is the expectation value of the square of the number of particles. Thus, the particle addition spectrum as a function of gate bias configurations represents diagrams in which non-zero values indicate the configurations that modify the total particle number. Additionally, the temperature is set to 10 K instead of 15 mK to obtain thicker transition lines in the addition spectrum, allowing the charge stability diagram to be computed by evaluating the addition spectrum for each configuration of the two plunger gate voltages.

3.8. QTCAD simulation complications

The iterative and computationally demanding nature of solving complex equations, together with the results sensitivity to mesh configurations and possible voltage settings are the main causes of a number of issues that

arise during the study. The convergence of the non-linear Poisson equation under strict error thresholds and the accurate tuning of plunger gates to attain symmetry in quantum dot structures are two crucial problems that arise during QTCAD simulations and are covered in this section. In order to maximize simulation accuracy guaranteeing accurate device behavior predictions, these issues must be solved.

3.8.1. Potential configuration and non-linear Poisson equation convergence
One primary issue with QTCAD is the slow convergence of the non-linear Poisson solution under a tolerable error threshold, which can be addressed by defining an optimal mesh with a large number of nodes inside and near the quantum layer in GMSH. The mesh is then refined through iterative adjustments of specific parameters during QTCAD's solution to the Poisson equation. Furthermore, establishing the right potential setup is essential for effectively confining the quantum dots. There is no standard technique for figuring out the precise configuration, it takes multiple simulations to discover the optimal one.

3.8.2. Plunger gate tuning
In an ideal double quantum dot system, supplying the same voltage to both plunger gates achieves perfect symmetry, but mesh asymmetries distort the potential profile, resulting in an uneven wavefunction distribution between the dots, as depicted in [9]. An offset voltage is added to the dot where the first stimulated level wavefunction is most localized in order to restore symmetry; if the voltage is set too high, the ground state wavefunction becomes primarily localized in the dot with the applied voltage. Similarly, in a four-dot system, potential corrections must be made to three dots to maintain even wavefunction distribution, which necessitates a stochastic method due to the lack of a standard procedure.

4. Results

This section presents the results obtained from the simulation of the heterostructure using QTCAD. Dirichlet boundary conditions are applied in the FEM solver to determine the required gate voltages that ensure the different wavefunctions distribution across the four dots, as shown in table 1.

V_{Yi} is applied to the *i*-Y gate, V_{Pil} to the *il*-plunger gate, V_{Bil} to the *il*-barrier gate, and V_{Ri} to the *i*-reservoir gate, where *R*, *L*, and *M* respectively denote right, left, and inter-dot, while *D* and *U* indicate down and up.

4.1. Four quantum dots configuration

The gate voltages are defined in such a way that the wavefunction is uniformly distributed across all four dots. V_{BRD} and V_{BLU} are higher than V_{BRU} and V_{BLD} since the latter correspond to the L barrier gates, which have a larger cross-section, as described in section 3.1. Furthermore, as discussed in section 3.8.2, offset voltages of 9.6534 mV, 30.4440 mV, and 27.2793 mV are applied to the left up, right up, and left down plungers, respectively, to achieve a symmetric potential profile.

4.1.1. Non linear Poisson equation results
Solving the Poisson equation allows the determination of the conduction band minimum, illustrated in figure 3(a), where the dark blue areas denote the four ohmic contacts (n+ doped regions), and the light blue regions on the sides show the two reservoir gates. Moreover, the simulation of the conduction band minimum vividly highlights the 3D confinement regions within the quantum layer. Furthermore, the classical electron population within the quantum layer is obtained from the Poisson solution, as shown in figure 3(b) for a cut at $z = 34.5$ nm. This image shows a uniform carrier distribution, with the exception of the four n+ doped regions (dark red) and the reservoir regions (light blue).

4.1.2. Single particle Schrödinger equation results
The eigenstates and eigenenergies are obtained from the solution of the single particle Schrödinger equation. In particular, figures 4(a) and (b) show the cuts on the *xy* plane inside the quantum layer, depicting the first two single particle eigenstates (bonding and antibonding eigenfunctions). Moreover, table 2 lists the eigenenergies of the first five eigenstates. It is interesting to note that the wavefunction does not completely vanish between the two upper dots or between the two lower dots, highlighting a strong coupling between the dots in each pair.

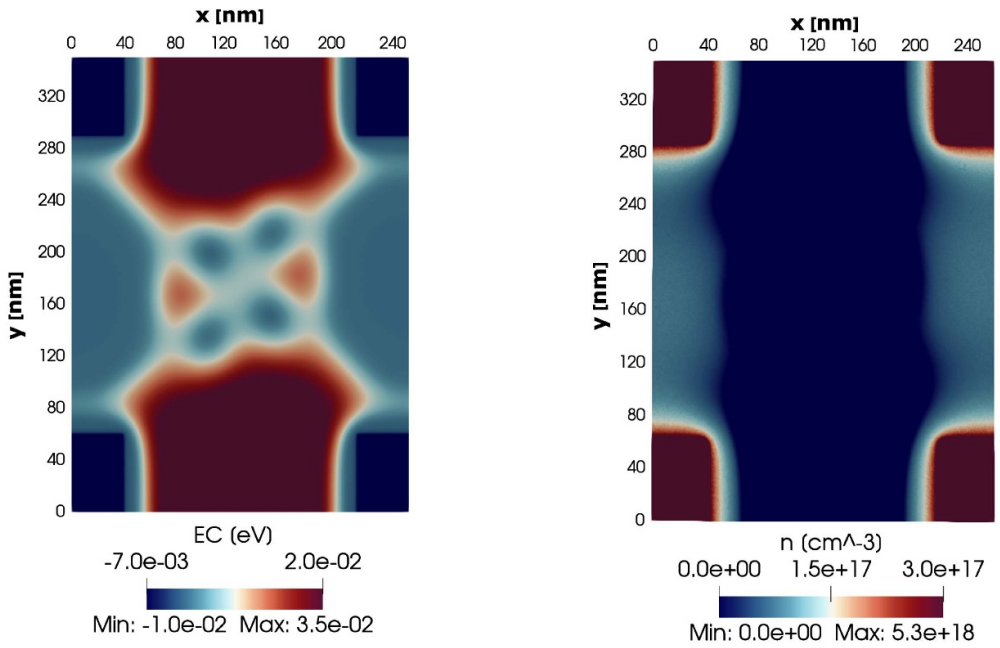
4.2. Upper and lower two dots configurations

The applied voltages need to be changed to isolate the various dot pairs; hence, a different potential configuration is employed for the upper dots pair and the lower dots pair, as depicted in table 1.

Since they sense the impact of the other voltage gates modifications, one should consider that the voltages applied to the plunger of interest are likewise altered. To correct for mesh asymmetries, an offset potential of

Table 1. All the different voltage configurations used to isolate the dots in the analysis are presented. Specifically, the first row describes the voltage configuration valid for section 4.1. The second and third rows correspond to the voltage configurations valid for section 4.2. The fourth and fifth rows refer to the voltage configurations valid for section 4.3. Finally, the last four rows describe the voltage configurations valid for section 4.4.

Configuration	V_{Y1} (mV)	V_{Y2} (mV)	V_{PLU} (mV)	V_{PRU} (mV)	V_{BLU} (mV)	V_{BMU} (mV)	V_{BRU} (mV)	V_{PLD} (mV)	V_{PRD} (mV)	V_{BLD} (mV)	V_{BMD} (mV)	V_{BRD} (mV)	V_{RL} (mV)	V_{RR} (mV)
Four dots	270	270	1260	1260	−530	−810	−520	1260	1260	−520	−810	−530	550	550
Upper dots	270	270	1220	1220	−560	−810	−470	200	200	190	200	200	550	550
Lower dots	270	270	200	200	200	200	190	1220	1220	−470	−560	−810	550	550
Left dots	270	270	1030	200	−500	200	190	1030	200	−470	200	200	550	550
Right dots	270	270	200	1030	200	200	−470	200	1030	190	200	−500	550	550
Upper right dot	270	270	280	850	280	850	−440	200	200	190	200	200	550	550
Lower left dot	270	270	200	200	200	200	190	850	280	−440	850	280	550	550
Upper left dot	270	270	680	220	−590	680	220	200	200	190	200	200	550	550
Lower right dot	270	270	200	200	200	200	190	220	680	220	680	−620	550	550



(a) Four quantum dot conduction band minimum

(b) Four quantum dot classical electrons density

Figure 3. the four quantum dots conduction band minimum and classical electrons density in the *xy* plane considering $z = 34.5$ nm, hence located inside the quantum layer, obtained by solving the non-Linear Poisson equation in QTCAD [29].

144.755 mV is applied to the V_{PRU} in the case of the two upper dots, and an offset potential of 151.181 mV is applied to the V_{PLD} for the two bottom dots. It is interesting to highlight that this two last configurations are symmetric and for this reason similar results are obtained.

4.2.1. Non linear Poisson equation results

From the solution of the non-linear Poisson equation, the conduction band minimum for the two different potential configurations is simulated, where the dark blue areas denote the four ohmic contacts (n+ doped regions), and the light blue regions on the sides denote the two reservoir gates.

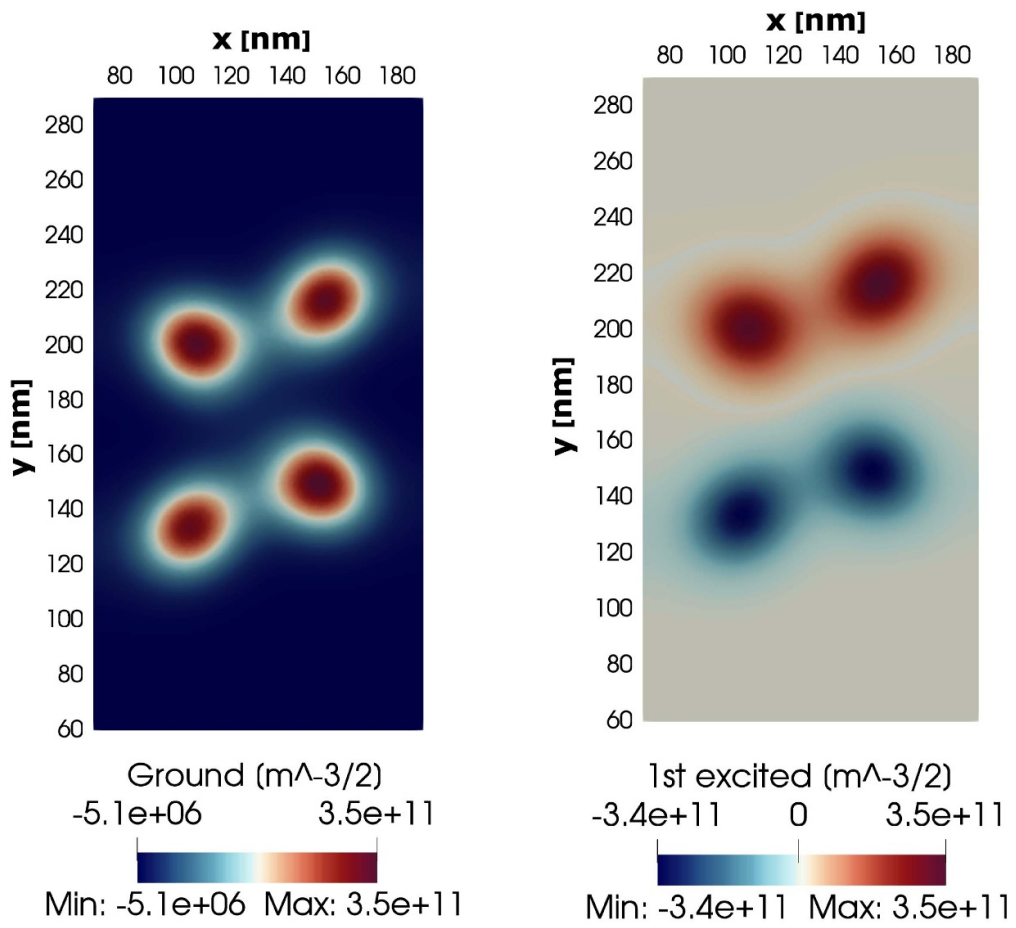
Specifically, figures 5(a) and (b) represents the conduction band minimum for both dots pairs in the *xy* plane considering $z = 34.5$ nm. Moreover, the simulation of the conduction band minimum vividly highlights the 3D confinement regions within the quantum layer. Finally, the behavior of the conduction band minimum along a specific axis passing through the two dots forming each pair for $z = 34.5$ nm, and for different combinations of dots, is shown in figures 6(a) and (b). The height of the inter-dot barrier for both pairs is computed as the difference between the maximum of the inter-dot confinement potential and the minimum of the two dot valleys. In both figures, the barrier height is approximately 3 meV, indicating that the dots are well-defined and isolated. Furthermore, the conduction band minimum profile, in both configurations, shows the anticipated similarity.

4.2.2. Single particle Schrödinger equation results

The solution of the single particle Schrödinger equation allows the determination of eigenspectra. Specifically, figures 7(a), (b), 8(a) and (b) show the cuts on the *xy* plane inside the quantum layer, depicting the bonding and antibonding eigenfunctions and revealing an equal distribution of the wavefunction over the dots for the two cases. Additionally, tables 3 and 4 list the eigenenergies of the first five eigenstates for both settings.

The last result obtained through this analysis is the approximation of the tunneling coefficient between the two pair dots. Due to the symmetry of both the configurations, the approximation value is almost equal, and moreover, considering equation (4), the computed value is:

$$t_0 \approx 100\,\mu\mathrm{eV} \implies 24.2\,\mathrm{GHz}. \tag{10}$$



(a) Bonding single particle eigenfunction in the xy plane

(b) Antibonding single particle eigenfunction in the xy plane

Figure 4. Single particle bonding and antibonding eigenfunctions in the *xy* plane located at $z = 34.5$ nm, hence inside the quantum layer, for the four quantum dot heterostructure. Both are obtained by solving the single particle Schrödinger equation in QTCAD [29].

Table 2. Eigenenergies for the first five states of the four quantum dot heterostructure obtained by solving the single particle Schrödinger equation in QTCAD [29].

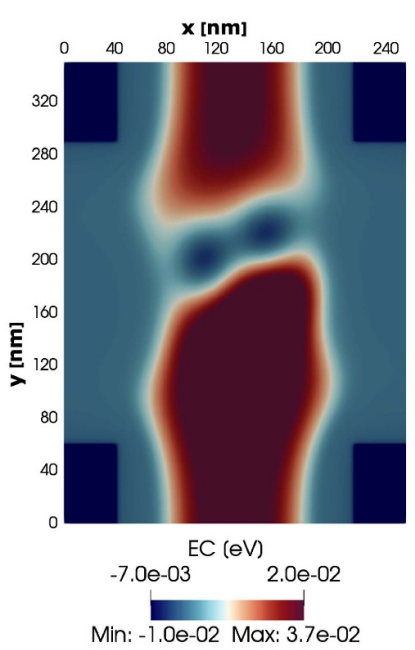
Energy level	Energy (meV)
0	6.9283
1	6.9542
2	7.5381
3	7.5867
4	9.1835

4.2.3. Lever arm

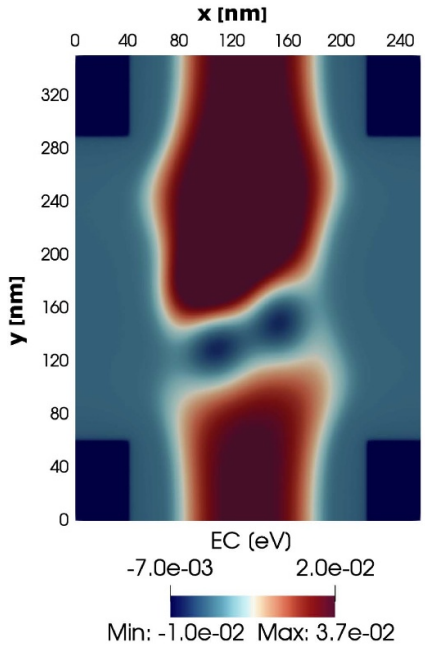
As described in section 3.5, the two lever-arm matrices are obtained through simulations, as shown in tables 5 and 6. These matrices are computed by considering five quantum states, as this number is sufficient to obtain accurate lever arm values for the first two states, which are the ones of interest. Calculations are performed incrementing the voltage of 100 μV at 15 mK.

4.2.4. Multi particle Schrödinger equation results

Considering the perturbative method, the approximation yields invalid results for the exchange interaction energy due to the strong Coulomb interaction between the dots. As discussed in section 3.6, the off-diagonal elements of the Coulomb matrix cannot be neglected since they are of the same order of magnitude as the diagonal elements. Hence, only the value obtained using the exact diagonalization method is reported, yielding an exchange interaction energy of approximately $J \approx 5.75$ meV $\implies$ 139 MHz. This value underscores the strong coupling between the two dots in both configurations, as previously indicated by the

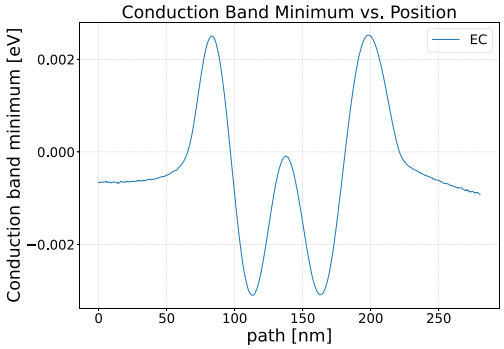


(a) Upper dots pair 2D conduction band minimum

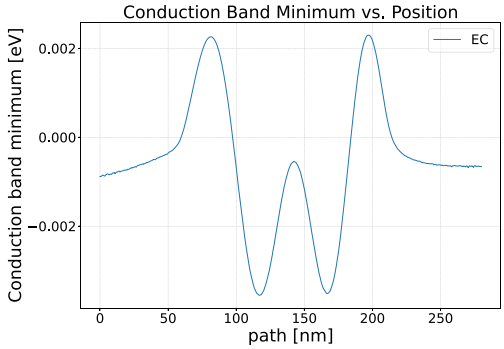


(b) Lower dots pair 2D conduction band minimum

Figure 5. The upper and lower dots pairs conduction band minima in the xy plane considering $z = 34.5$ nm, hence located inside the quantum layer, is obtained by solving the non-linear Poisson equation in QTCAD [29].



(a) Upper dots pair 1D Conduction Band Minimum



(b) Lower dots pair 1D Conduction Band Minimum

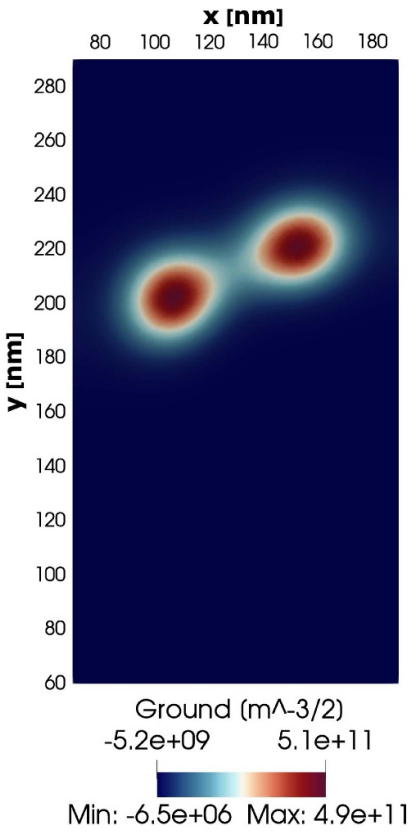
Figure 6. The dots pairs conduction band minimum for different x and y positions at $z = 34.5$ nm obtained by solving the non-linear Poisson equation in QTCAD [29]. On the left 6(a), the conduction band minimum is shown along a line passing through the points $(x = 0, y = 166)$ nm and $(x = 260, y = 271)$ nm, which define the line passing through the minima of the two dots. On the right 6(b), the conduction band minimum is shown along a line passing through the points $(x = 0, y = 80)$ nm and $(x = 260, y = 184)$ nm, which define the line passing through the minima of the two dots.

tunneling coupling approximation. Due to the symmetry of the configurations, the resulting values are nearly identical.

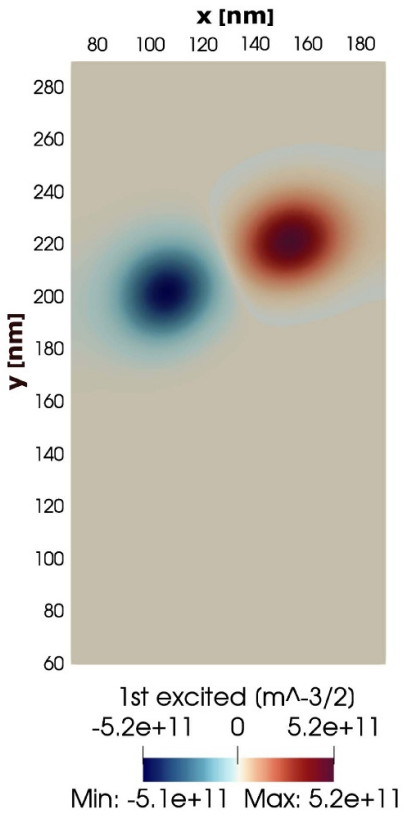
4.2.5. Charge stability diagram results

The charge stability diagram is computed by taking into account the addition spectrum for each configuration of the two plunger gate voltages. Specifically, the plunger gate voltages vary from -350 to 2000 mV with a zero source-drain voltage.

From figures 9(a) and (b), two cases for the upper dots pair configuration can be observed: one for low coupling between the dots (inter-dot barrier gate voltage equal to -0.8 V) and one for high coupling between the dots (inter-dot barrier gate voltage equal to -0.5 V). In the low coupling case, the two dots operate almost independently, where alterations in each gate voltage solely influence the corresponding dot's behavior. Nevertheless, the presence of triple points in the transition of the low coupling charge stability



(a) Upper Bonding single particle eigenfunction in the xy plane



(b) Upper Antibonding single particle eigenfunction in the xy plane

Figure 7. Single particle bonding and antibonding eigenfunctions in the *xy* plane located at $z = 34.5$ nm, hence inside the quantum layer, for the upper dots pair. Both are obtained by solving the single particle Schrödinger equation in QTCAD [29].

diagram suggests a small interdependence between the dots in this scenario as well. A triple point in gate voltage space occurs when the energy levels of three separate charge configurations become degenerate, enabling an electron to tunnel freely between two quantum dots and the reservoir without any energy cost. On the other hand in the high coupling scenario, the voltage applied to single dot gate directly impacts the behavior of the other dot through this capacitive interaction.

In conclusion, the results highlight that the simulated charge stability diagrams are physically plausible and compatible with the ones reported in [30]. Similar scenario is observed for the lower dots pair, the only differences are that the interdot barrier gate voltage is V_{BMD}, and in the low coupling case, the diagram shown in figure 10 exhibits slight variations compared to the one for the upper dot pair. These differences arise due to the distinct lever arm behavior, as discussed in section 4.2.3.

4.3. Left and right two dots configurations

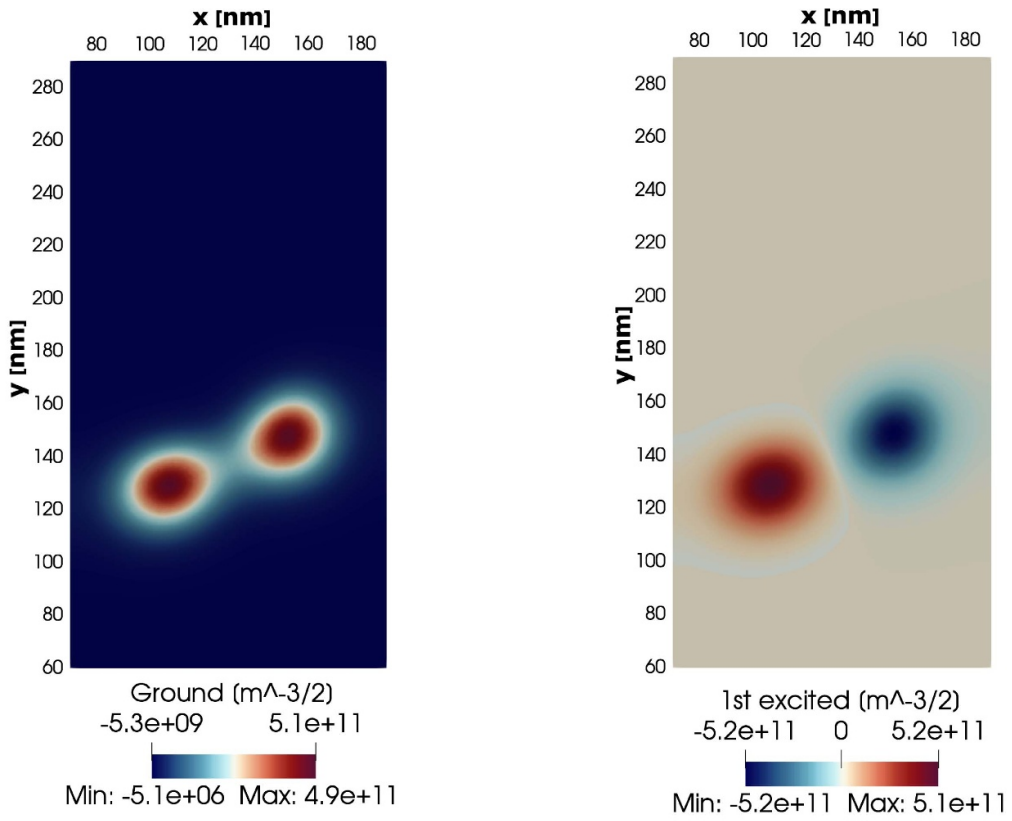
The different potential configurations used for the upper and lower dot pairs are described in table 1, and they are symmetric with respect to each other. To compensate for mesh asymmetries, an offset potential of 33.7538 mV is applied to V_{PLU} for the two left dots, while 29.8764 mV is applied to V_{PRU} for the two right dot configuration.

4.3.1. Non linear Poisson equation results

Similarly to section 4.2.1, the 1D and 2D conduction band minimum (represented respectively in figures 12 and 11) for the right and left dot pairs are calculated. In particular, from figures 12(a) and (b), the barrier height is approximately 9 meV, indicating a higher barrier compared to one of section 4.2.1. Additionally, the conduction band minimum profile in both configurations exhibits the expected similarity.

4.3.2. Single particle Schrödinger equation results

The eigenstates in the *xy* plane inside the quantum layer are shown in figure 13 and in figure 14. These cuts represent the bonding and antibonding eigenfunctions and exhibit an equal distribution of the wavefunction



(a) Lower Bonding single particle eigenfunction in the xy plane

(b) Lower Antibonding single particle eigenfunction in the xy plane

Figure 8. Single particle bonding and antibonding eigenfunctions in the *xy* plane located at $z = 34.5$ nm, thus inside the quantum layer, for the lower dots pair. Both are obtained by solving the single particle Schrödinger equation in QTCAD [29].

Table 3. Eigenenergies associated the first five states of the quantum dot upper pair obtained by solving the single particle Schrödinger equation in QTCAD [29].

Energy level	Energy (meV)
0	3.4866
1	3.6151
2	5.6966
3	6.4061
4	7.3117

Table 4. Eigenenergies for the first five states of the quantum dot lower pair obtained by solving the single particle Schrödinger equation in QTCAD [29].

Energy level	Energy (meV)
0	3.1446
1	3.2790
2	5.3584
3	6.1073
4	7.0033

over the dots for the two cases. The eigenenergies of the first five eigenstates for both configurations are also listed in tables 7 and 8.

The tunneling approximation coefficient is almost equivalent due to the configuration symmetry, and the calculated value is:

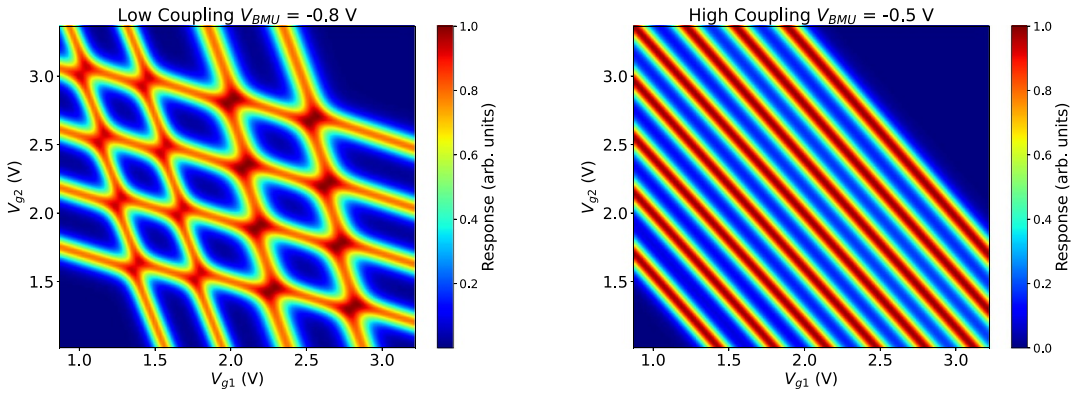
$$t_0 \approx 1.97\,\mu\text{eV} \implies 477\,\text{MHz}. \tag{11}$$

Table 5. Lever arm matrix for the two upper dot for the first five states, considering the two upper plungers gates and the inter-dot barrier gate between them, obtained by solving the single particle Schrödinger equation in QTCAD [29].

Energy level	α_{PLU}	α_{BMU}	α_{PRU}
0	1.2055×10^{-2}	1.7644×10^{-2}	2.5698×10^{-2}
1	3.3574×10^{-2}	1.9750×10^{-2}	1.2391×10^{-2}
2	8.723×10^{-3}	1.2241×10^{-2}	1.9764×10^{-2}
3	2.4278×10^{-2}	1.1888×10^{-2}	7.786×10^{-3}
4	1.9375×10^{-2}	1.8246×10^{-2}	1.7610×10^{-2}

Table 6. Lever arm matrix for the two lower dot for the first five states, considering the two lower plungers gates and the inter-dot barrier gate between them, obtained by solving the single particle Schrödinger equation in QTCAD [29].

Energy level	α_{PLD}	α_{BMD}	α_{PRD}
0	2.5249×10^{-2}	1.5228×10^{-2}	1.0713×10^{-2}
1	1.1369×10^{-2}	1.7708×10^{-2}	3.4742×10^{-2}
2	2.0371×10^{-2}	1.1800×10^{-2}	8.455×10^{-3}
3	6.556×10^{-3}	9.981×10^{-3}	2.3998×10^{-2}
4	6.458×10^{-3}	9.666×10^{-3}	2.2343×10^{-2}



(a) Upper Charge Stability Diagram with V_{BMU} equal to -0.8 V

(b) Upper Charge Stability Diagram with V_{BMU} equal to -0.5 V

Figure 9. Charge stability diagrams for the heterostructure obtained in QTCAD [29]. On the left 9(a), the charge stability diagrams for the upper dots pair with V_{BMU} equal to -0.8 V, resulting in low coupling between the dots, so they behave almost independently. On the right 9(b), the charge stability diagrams for the upper dots pair with V_{BMU} equal to -0.5 V, resulting in high coupling between the dots, which makes them to behave more like a single dot.

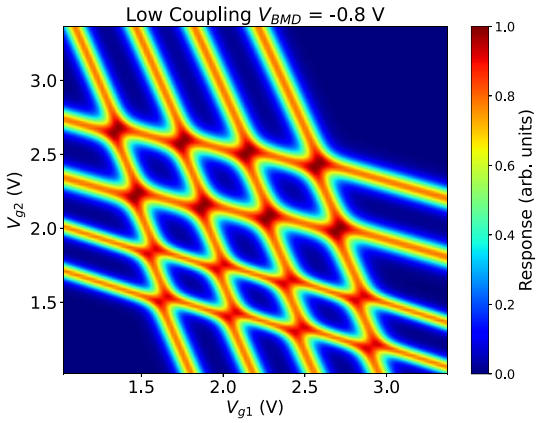
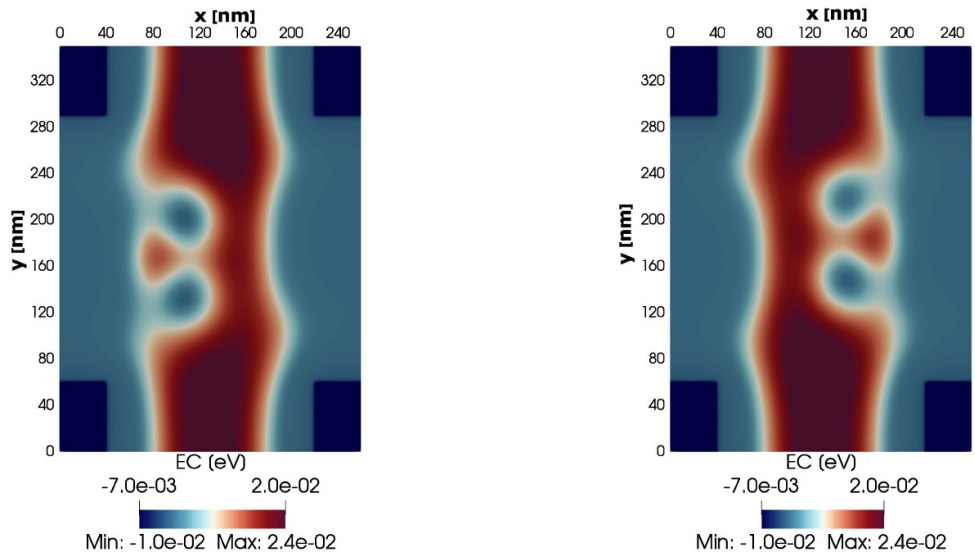


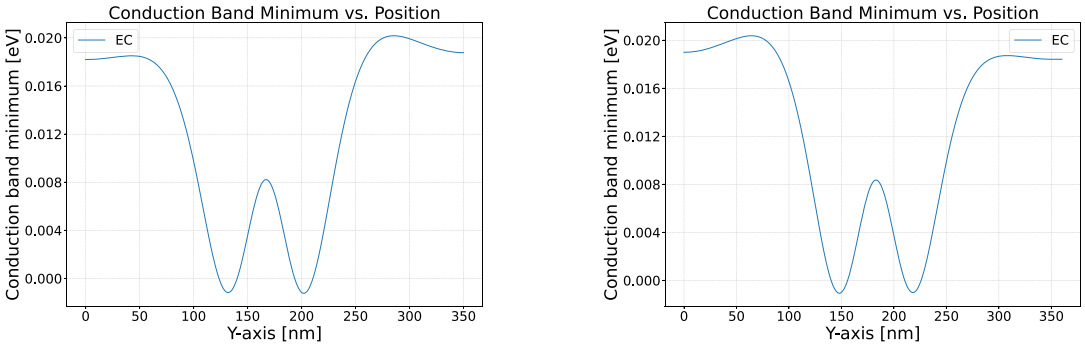
Figure 10. Charge stability diagrams for the lower dots pair obtained using QTCAD [29]. The V_{BMD} set to -0.8 V, which results in low coupling between the quantum dots. In this regime, the dots behave almost independently.



(a) Left dots pair 2D conduction band minimum.

(b) Right dots pair 2D conduction band minimum.

Figure 11. The left and right dots pair conduction band minima in the *xy* plane considering $z = 34.5$ nm, obtained by solving the non-linear Poisson equation in QTCAD [29].



(a) Left dots pair 1D conduction band minimum.

(b) Right dots pair 1D conduction band minimum.

Figure 12. The left and right dots pairs conduction band minimum along $\hat{y}$ axis considering $z = 34.5$ nm and different x, obtained by solving the non-linear Poisson equation in QTCAD [29]. On the left 12(a), the conduction band minimum is shown along the $\hat{y}$-axis considering $x = 105$ nm, in this way the axis pass trough the two left dots. On the right 12(b), the conduction band minimum along the $\hat{y}$-axis considering $x = 155$ nm, in this way the axis passes trough the two right dots.

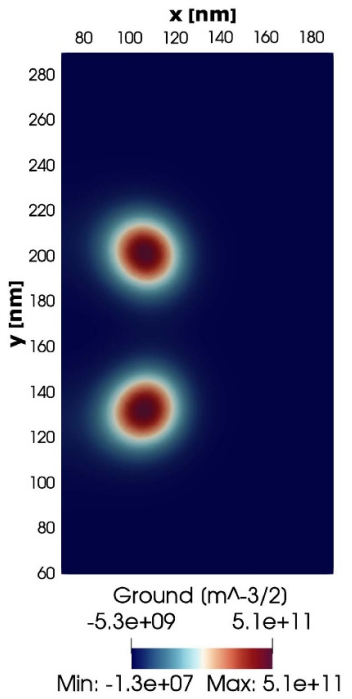
As expected, this value is smaller compared to the one calculated for the upper and lower pairs. This difference arises because the interdot barrier is higher for the left and right dot pairs.

4.3.3. Lever arm

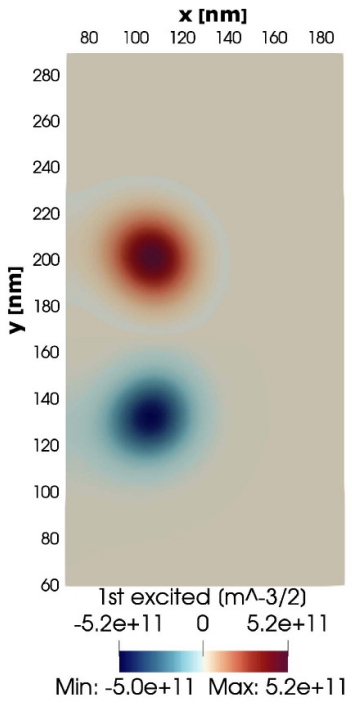
As described in section 3.5, the two lever arm matrices are obtained through simulations, as shown in tables 9 and 10. These matrices are computed by considering five quantum states, as this number is sufficient to obtain accurate lever arm values for the first two states, which are the ones of interest. Calculations are performed incrementing the voltage of 100 μV at 15 mK. Considering the symmetric configurations, the results of both are similar.

4.3.4. Multi particle Schrödinger equation results

For both configurations, the exchange interaction energy is calculated using both accurate diagonalization and perturbative methods since, unlike in section 4.2.4, the Coulomb interaction between the dots is not sufficiently intense to preclude the use of the perturbative method. The value obtained using the perturbative method is of the same order of magnitude as the one obtained using the exact diagonalization method, highlighting the validity of both approaches. Because of the symmetry of the configurations, the final values

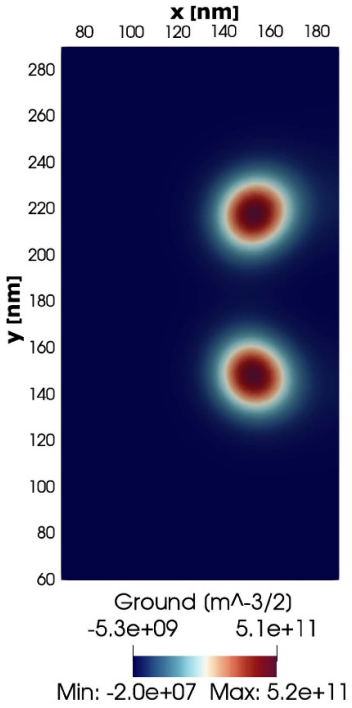


(a) Left bonding single particle eigenfunction in the xy plane.

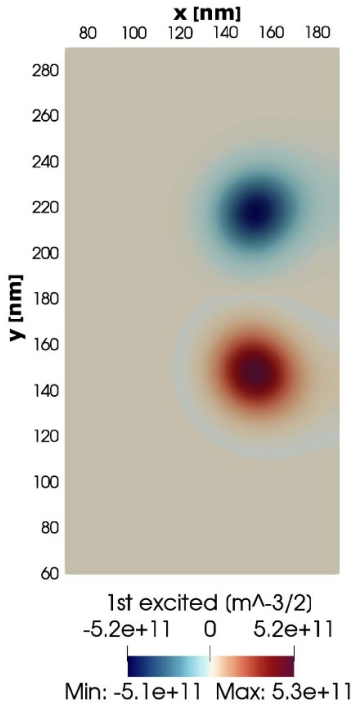


(b) Left antibonding single particle eigenfunction in the xy plane.

Figure 13. Single particle bonding and antibonding eigenfunctions in the *xy* plane located at $z = 34.5$ nm for the left dots pair. Both are obtained by solving the single particle Schrödinger equation in QTCAD [29].



(a) Right bonding single particle eigenfunction in the xy plane.



(b) Right antibonding single particle eigenfunction in the xy plane.

Figure 14. Single particle bonding and antibonding eigenfunctions in the *xy* plane located at $z = 34.5$ for the right dots pair. Both are obtained by solving the single particle Schrödinger equation in QTCAD [29].

Table 7. Eigenenergies for the first five states of the quantum dot left pair obtained by solving the single particle Schrödinger equation in QTCAD [29].

Energy level	Energy (meV)
0	6.4580
1	6.4597
2	9.1180
3	9.3923
4	9.8509

Table 8. Eigenenergies for the first five states of the quantum dot right pair obtained by solving the single particle Schrödinger equation in QTCAD [29].

Energy level	Energy (meV)
0	6.5590
1	6.5607
2	9.1946
3	9.4928
4	9.8718

Table 9. Lever arm matrix for the two left dot for the first five states, considering the two plungers gate and the inter-dot barrier gate of obtained by solving the single particle Schrödinger equation in QTCAD [29].

Energy level	α_{PLU}	α_{BLD}	α_{PLD}
0	3.5639×10^{-2}	4.1659×10^{-2}	3.5832×10^{-2}
1	1.9619×10^{-2}	3.7790×10^{-2}	1.9066×10^{-2}
2	1.0781×10^{-2}	4.2318×10^{-2}	3.3928×10^{-2}
3	3.7065×10^{-2}	3.1386×10^{-2}	1.2238×10^{-2}
4	5.640×10^{-3}	6.362×10^{-3}	4.135×10^{-3}

Table 10. Lever arm matrix for the two right dot for the first five states, considering the two plungers gate and the inter-dot barrier gate of obtained by solving the single particle Schrödinger equation in QTCAD [29].

Energy level	α_{PRU}	α_{BRU}	α_{PRD}
0	3.7359×10^{-2}	4.1816×10^{-2}	3.5436×10^{-2}
1	1.9408×10^{-2}	3.7821×10^{-2}	1.9392×10^{-2}
2	3.5195×10^{-2}	4.2462×10^{-2}	1.0572×10^{-2}
3	1.2330×10^{-2}	3.1197×10^{-2}	3.6778×10^{-2}
4	4.189×10^{-3}	6.317×10^{-3}	5.582×10^{-3}

are nearly identical. Following this analysis, it is found that the exchange interaction energy is $J \approx 6.08$ peV $\implies$ 147 kHz using the exact diagonalization method and $J \approx 5.71$ peV $\implies$ 138 kHz using the perturbative method. As expected, these values are lower than those found for the up and down pairs of dots, as the interdot barrier is higher in the left and right dot pairs.

4.3.5. Charge stability diagram results

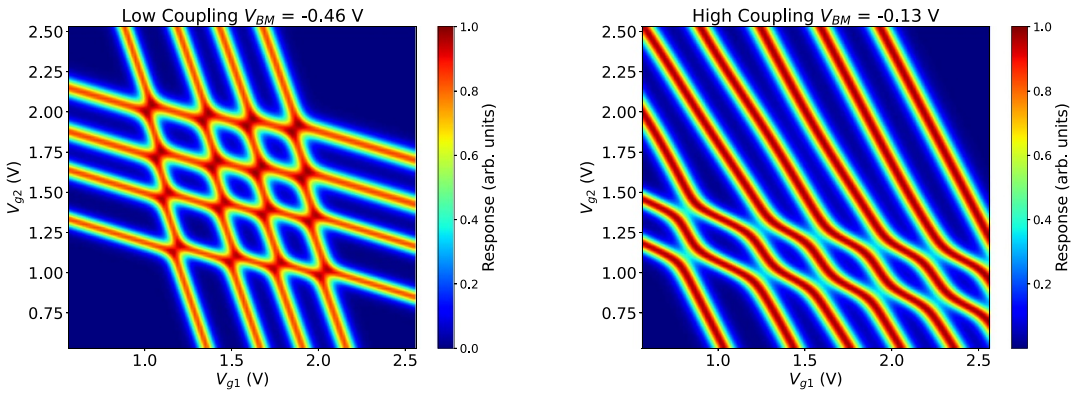
The charge stability diagrams are calculated by changing the plunger gate voltages from −500 to 1500 mV with a zero source-drain voltage. From figures 15(a) and (b), the high coupling and low coupling case, for the two left dots are represented. They have similar behavior to the one, described in section 4.2.5, of the upper and down dots pairs.

Analogous consideration can be extracted analyzed the right pair dots, as they are symmetric and share the same lever arm. For both the left and right dot pairs, the interdot barrier voltage used in the Poisson and Schrödinger calculations is nearly identical to that used in the low coupling case.

In contrast, the interdot barrier voltage considered in the Poisson and Schrödinger results is significantly higher than in the low-coupling case. This observation further highlights the stronger coupling present in the upper and lower dot pairs compared to the left and right.

4.4. Single dot configurations

A single dot analysis is conducted, isolating each of the four dots to perform a one-dimensional transport analysis, enabling the computation of Coulomb peaks and Coulomb diamonds. The four voltage



(a) Left dots pair charge stability diagram with V_{BLD} equal to -0.46 V

(b) Left dots pair Charge Stability Diagram with V_{BLD} equal to -0.13 V

Figure 15. Charge stability diagrams for the left dots pair obtained in QTCAD [29]. On the left 15(a), the charge stability diagrams for the left dots pair with V_{BLD} equal to -0.46 V, resulting in low coupling between the dots, so they behave almost independently. On the right 15(b), the charge stability diagrams for the left dots pair with V_{BLD} equal to -0.13 V, resulting in high coupling between the dots, causing them to behave more like a single dot.

configuration are reported in table 1. As observed, the applied voltage is the same for the dots that are symmetric with respect to the center.

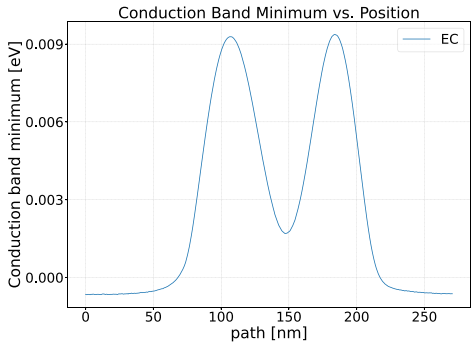
4.4.1. Non linear Poisson equation results

The results for each single-dot configuration related to the solution of the non-linear Poisson equation are reported in figure 16. The results highlight the symmetry between the upper right single dot and the lower left dot, as well as the symmetry between the upper left single dot and the lower right single dot. In the upper left and lower right single-dot configurations, one of the barriers is significantly thinner than the other due to the device layout. In contrast, for the upper right and lower left single-dot configurations, the two barriers have nearly equal thickness.

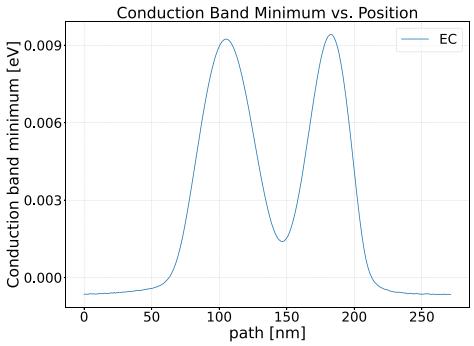
4.4.2. Coulomb peaks results

The process outlined in section 3.7.1 is used to represent the Coulomb peaks for every configuration, as shown in figure 19. In particular, symmetric configurations produce results that are comparable, even though only four states are taken into account. Since no magnetic field is applied, the first peak refers to the single electron ground eigenstate and contains both contributions of spin up and down. Moreover, the energy required to add a second electron is equal to the difference between the ground-state energy of the system with one electron and the ground-state energy of the system with two electrons (called charging energy). Thus the second peak is associated to the ground state with two electrons. The same principle applies when adding more electrons. Using the featureless approximation, the current entering the device is simulated as the plunger voltage changes with a vanishing source-drain voltage ($V_{\mathrm{DS}} = 1$ mV) and a lever arm of 0.00884, the plunger voltage for the left upper and right lower dots is adjusted between 0.3 V and 4 V.

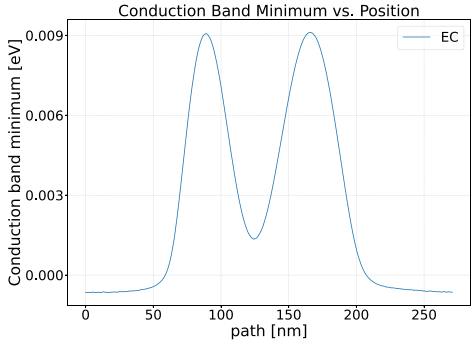
Likewise, for the lower left and upper right dots, the plunger voltage is adjusted between 0 V and 4 V. The source-drain voltage vanishes ($V_{\mathrm{DS}} = 1$ mV), but the lever arm is 0.04407. Since the simulation is performed considering four states with degeneracy two, eight peaks are expected. In figures 20(a) and (b), the visible peaks are seven because the fourth and fifth peaks are so close that they partially overlap and a single wider peak is observed. In figures 20(a) and (d), only five peaks are observed because the single-dot energy levels are higher due to the weaker confinement created by the barrier gates. As a result, the peak positions occur at higher energies, extending beyond the plunger voltage range. Nevertheless, the first two peaks are the ones of interest for spin qubits implementation. Also for these two configurations, the smallest distance is between the fourth and fifth peaks, and they partially overlap forming a large peak. As described in section 3.7.1, the current is scaled by the one obtained using the NEGF formalism. The four local densities of states, depicted in figure 17 and in figure 18, are used to adjust the bias window so that only the first lobe falls within it. This ensures operation in the sequential tunneling regime. The first lobe of the lower left dot and the upper right dot is below the conduction band minimum. Since the plots represent a line cut of a 3D problem, it implies that the band edge minimum, calculated by solving the Poisson equation using the NEGF formalism, may occur at a different location in the device than the one computed using the Poisson solver described in



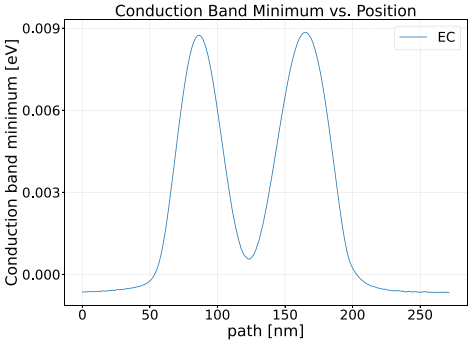
(a) Right upper dot 1D conduction band minimum



(b) Right lower dot 1D conduction band minimum

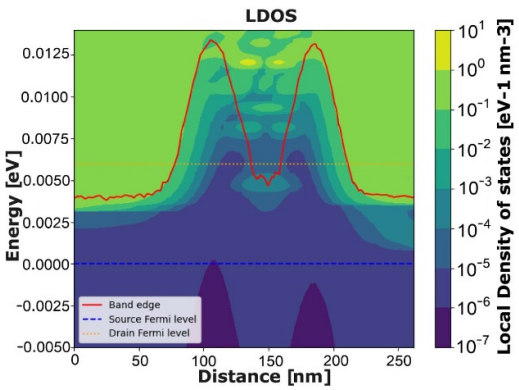


(c) Left upper dot 1D conduction band minimum

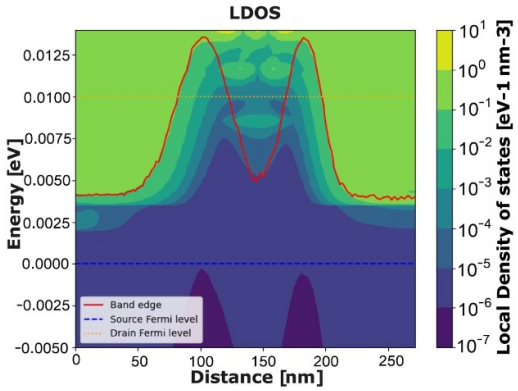


(d) Left lower dot 1D conduction band minimum

Figure 16. 1D conduction band minimum for the four single dot considering $z = 35.5$ nm, obtained by solving the non-linear Poisson equation in QTCAD [29]. In figure 16(a) shows the right upper dot 1D conduction band minimum along a line passing through the points $(x = 0, y = 166)$ nm and $(x = 260, y = 261)$ nm, which define the line passing through the minima of the dot. Figure 16(c) shows the left upper dot 1D conduction band minimum along a line passing through the points $(x = 0, y = 164)$ nm and $(x = 260, y = 245)$ nm, which define the line passing through the minima of the dot. Figure 16(b) shows the right lower dot 1D conduction band minimum along a line passing through the points $(x = 0, y = 112\ )$ nm and $(x = 260, y = 169)$ nm, which define the line passing through the minima of the dot. Figure 16(d) shows the left lower dot 1D conduction band minimum along a line passing through the points $(x = 0, y = 90)$ nm and $(x = 260, y = 183\ )$ nm, which define the line passing through the minima of the dot.



(a) Right Upper dot LDOS

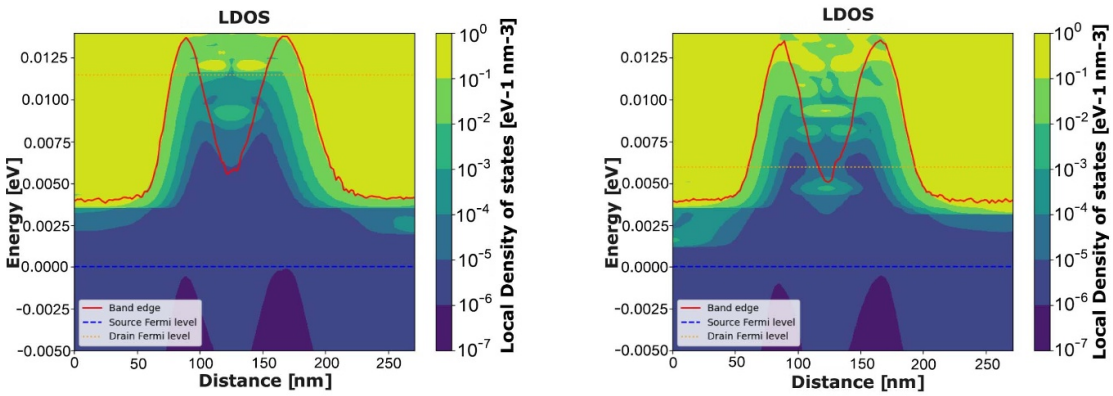


(b) Right Lower dot LDOS

Figure 17. LDOS for the two right single dot obtained by using the NEGF formalism in QTCAD [29].

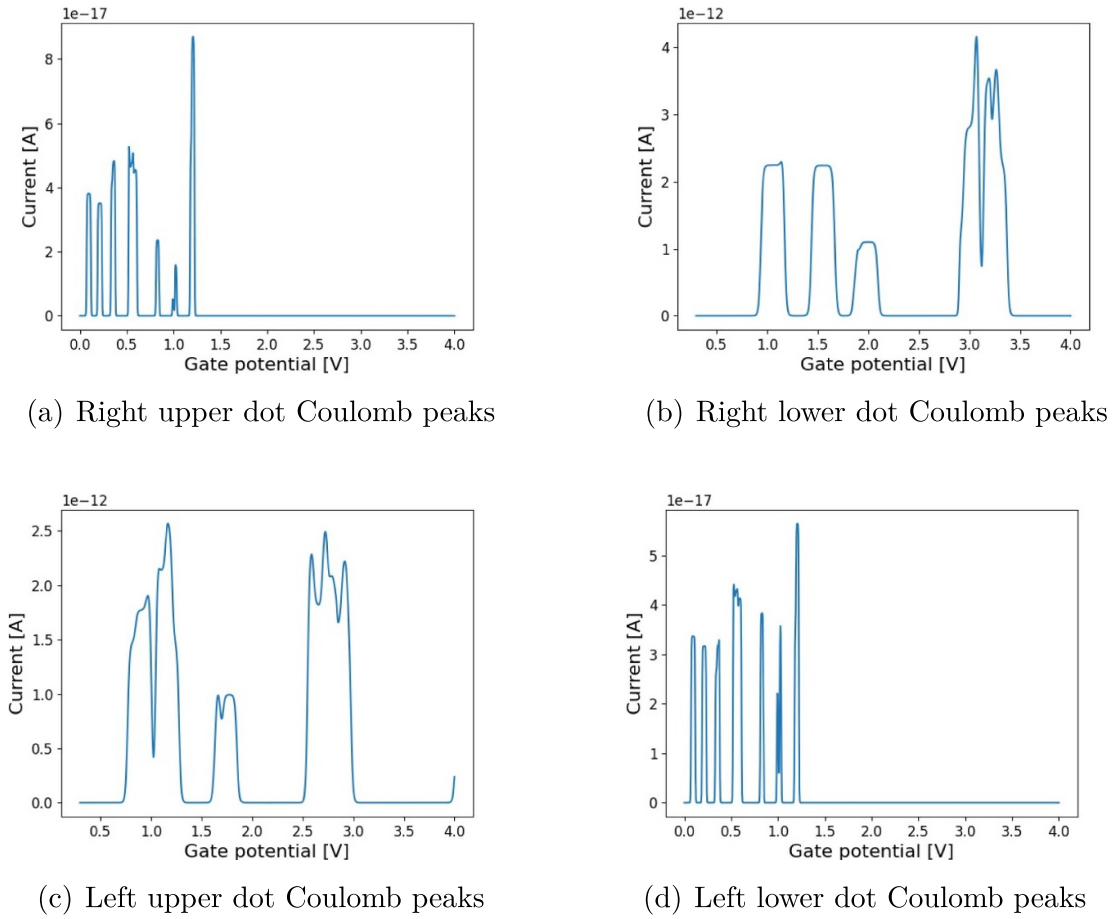
section 2.1. However, this is not an issue, as the key consideration is to ensure that the device operates in the sequential tunneling regime.

Lastly, the NEGF current values vary between the two pairs of symmetric configurations, with the one involving the left upper dot and the right lower dot exhibiting a higher current. This is because the barrier closer to the contact is thinner in the former configuration; as a result, the lobe rises higher, suggesting that the electron is less localized, leading to an increase in current. The positions of the lobes and the lever arm



(a) Left Upper dot LDOS (b) Left Lower dot LDOS

Figure 18. LDOS for the two left single dot obtained by using the NEGF formalism in QTCAD [29].



(a) Right upper dot Coulomb peaks (b) Right lower dot Coulomb peaks

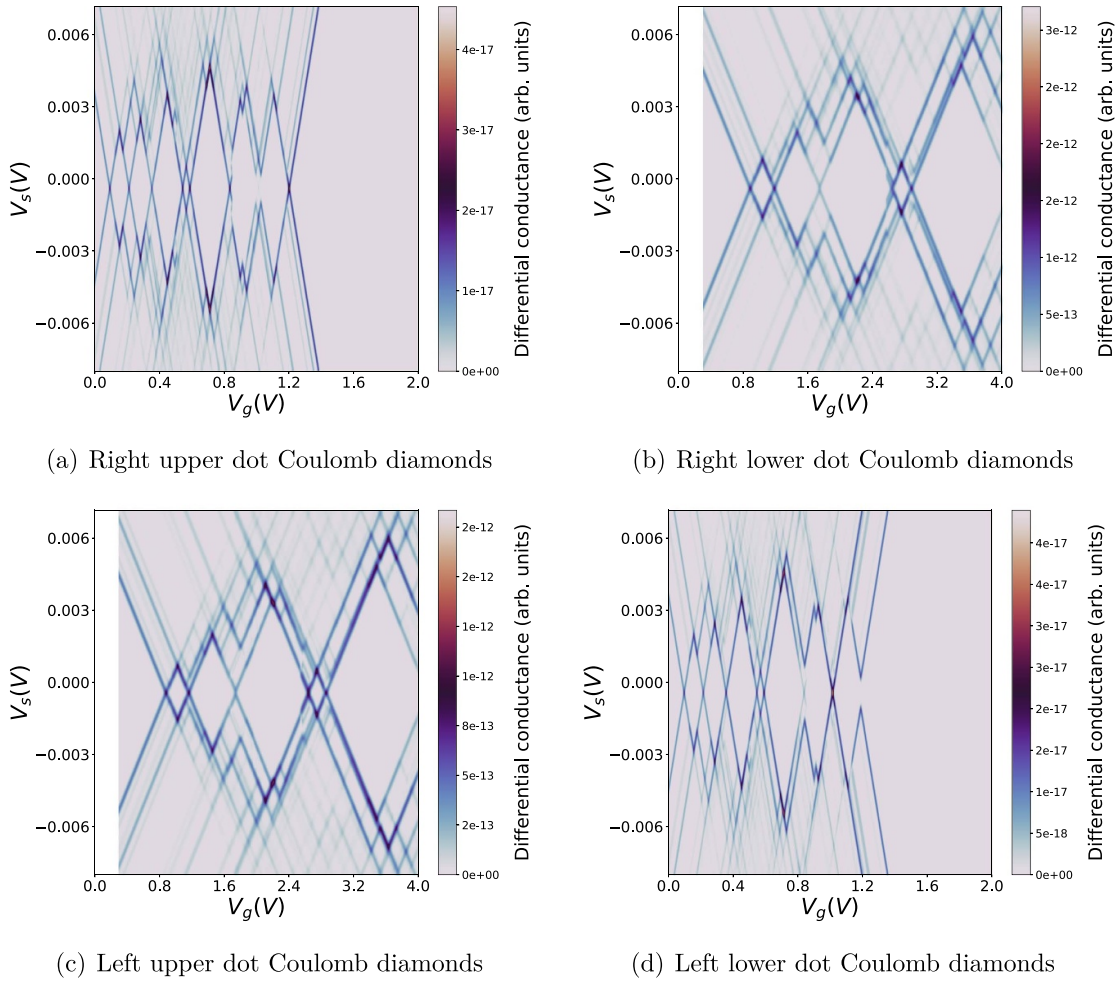
(c) Left upper dot Coulomb peaks (d) Left lower dot Coulomb peaks

Figure 19. Coulomb peaks for the four single dot obtained in QTCAD [29].

values explain why the left upper and right lower peaks differ so much from the right upper and left lower ones.

4.4.3. Coulomb diamonds results

The Coulomb diamonds for the four single dot configurations are calculated and shown in figure 20. In particular, the lever arm for the lower right and upper left dots is 0.00884, the source-drain voltage sweeps between −8 mV and 8 mV, and the plunger gate voltage sweeps between 0.3 V and 4 V. Similarly, the source-drain voltage varies between −8 mV and 8 mV for the lower left and upper right dots, while the lever arm is 0.04407. The plunger voltage is additionally modified between 0 V and 4 V. Like the Coulomb peaks,



(a) Right upper dot Coulomb diamonds

(b) Right lower dot Coulomb diamonds

(c) Left upper dot Coulomb diamonds

(d) Left lower dot Coulomb diamonds

Figure 20. Coulomb diamonds for the four single dot obtained in QTCAD. [29].

the results for the symmetric configurations are similar. Furthermore, in figures 20(a) and (d), seven diamonds are observed, representing the Coulomb blockade regions for one to seven electrons, while two half-diamonds correspond to the cases of zero and eight electrons. Specifically, the smallest diamond in both figures corresponds to the Coulomb blockade regime with four electrons. In fact, the horizontal dimension of this diamond is equal to the spacing between the fourth and fifth Coulomb peaks, which, as described in section 4.4.2, is the smallest. Only five diamonds can be seen in figures 20(b) and (c) because, as discussed in section 4.4.2, the final three Coulomb peaks positions are beyond the plunger voltage range. Finally, because of the extremely small distance between the fourth and fifth Coulomb peaks, the smallest diamond is associated with the fourth electron Coulomb blockade regime.

5. Conclusion

The goal of this work is to perform these simulations to evaluate the device's feasibility for real-world applications and efficiently assess its response to structural parameter modifications. Consequently, structural changes can be made by simply altering the simulation code, avoiding the need for repetitive and expensive lithographic processes.

Moreover, the simulation of the tunneling coefficient approximation and the interaction exchange energy for distinct dot pairs provides insights into the interdependence among the dots, which is crucial to control qubits made with this device. Regarding the transport analysis, it validates the single-electron regime, which is critical for precise control and manipulation of qubits implemented through the four quantum dot heterostructure. In particular, the size and the position of Coulomb diamonds, as well as the spacing between Coulomb peaks, provide the quantum dot energy levels and electron interactions. Furthermore, in low-coupling conditions, the charge stability diagram shows non negligible interdependence between the

dots, even when separated by a large inter-dot barrier. A full understanding of these characteristics is necessary for the precise implementation of quantum logic gates within this heterostructure, ensuring stable qubit control and operation.

Using on the results presented here, one interesting future direction is to extend the Fermi–Hubbard model, described in [9], to define four qubits and simulate more complex logic gates with the four quantum dots structure. At the same time, exploring hole spin qubits in germanium quantum dots within QTCAD presents another intriguing possibility. However, solving the Schrödinger equation for holes is particularly challenging because physics is predominantly influenced by the valence band maximum, which is degenerate or nearly degenerate at the Γ point in semiconductors with a diamond lattice. This complexity makes theoretical modeling even more critical, as it can provide valuable predictions before experimental implementation. Finally, comparing simulation results with experimental data would not only help validate the former but also support an iterative experimental-simulation loop. Although QTCAD idealizes many aspects, the obtained results serve as a valuable starting point for understanding device behavior before experimental realization in the laboratory.

Data availability statement

All data that support the findings of this study are included within the article (and any supplementary files).

Acknowledgments

We thank Nanoacademic Technologies Inc. for their support during the development of our work.

ORCID iDs

Giovanni Pedicini 0009-0003-3627-7255
Antonio Tudisco 0009-0000-7447-1882
Mario Cignoni 0000-0002-5702-2505
Mariagrazia Graziano 0000-0002-8721-9990
Fabrizio Riente 0000-0003-4147-1098

References

[1] Pedersen L H, Møller N M and Mølmer K 2007 *Phys. Lett. A* **367** 47–51
[2] Burkard G, Ladd T D, Pan A, Nichol J M and Petta J R 2023 *Rev. Mod. Phys* **95** 025003
[3] Morello A *et al* 2010 *Nature* **467** 687–91
[4] Weber J R, Koehl W F, Varley J B, Janotti A, Buckley B B, de Walle C G V and Awschalom D D 2010 *Proc. Natl Acad. Sci.* **107** 8513–8
[5] Gorman J, Hasko D and Williams D 2005 *Phys. Rev. Lett.* **95** 090502
[6] Unseld F K, Meyer M, Madzik M T, Borsoi F, de Snoo S L, Amitonov S V, Sammak A, Scappucci G, Veldhorst M and Vandersypen L M K 2023 *Appl. Phys. Lett.* **123** 084002
[7] Kriekouki I, Beaudoin F, Philippopoulos P, Zhou C, Lemyre J C, Rochette S, Mir S, Barragan M J, Pioro-Ladrière M and Galy P 2022 *Solid-State Electron.* **194** 108355
[8] Foulk N L and Das Sarma S 2024 *Phys. Rev. B* **110** 205428
[9] Costa D, Simoni M, Piccinini G and Graziano M 2023 *IEEE Access* **11** 98875–913
[10] Geuzaine C and Remacle J F 2009 *Int. J. Numer. Methods Eng.* **79** 1309–31
[11] Kriekouki I, Philippopoulos P, Beaudoin F, Mir S, Barragan M J, Pioro-Ladrière M and Galy P 2023 *Solid-State Electron.* **209** 108777
[12] Winkler R, Papadakis S, De Poortere E and Shayegan M 2003 *Spin-Orbit Coupling in two-Dimensional Electron and Hole Systems* vol 41 (Springer)
[13] Tokura Y, van der Wiel W G, Obata T and Tarucha S 2006 *Phys. Rev. Lett.* **96** 047202
[14] Mohiyaddin F *et al* 2020 Tcad-assisted multiphysics modeling & simulation for accelerating silicon quantum dot qubit design *2020 Int. Conf. on Simulation of Semiconductor Processes and Devices (SISPAD)* (IEEE) pp 253–6
[15] Güçlü A, Sun Q F, Guo H and Harris R 2002 *Phys. Rev. B* **66** 195327
[16] Bednarek S, Szafran B and Adamowski J 2000 *Phys. Rev. B* **61** 4461
[17] Hensgens T, Fujita T, Janssen L, Li X, Van Diepen C, Reichl C, Wegscheider W, Das Sarma S and Vandersypen L M 2017 *Nature* **548** 70–73
[18] Mielke A Autumn School organized by the Forschungszentrum Jülich and the German Research School for Simulation Sciences at Forschungszentrum Jülich
[19] Bruus H and Flensberg K 2004 *Many-Body Quantum Theory in Condensed Matter Physics: An Introduction* (OUP Oxford)
[20] Prentki R J, Harb M, Zhou C, Philippopoulos P, Beaudoin F, Michaud-Rioux V and Guo H 2022 *Solid-State Electron.* **197** 108438
[21] Prentki R J, Fehse F, Philippopoulos P, Zhou C, Guo H, Korkusinski M and Beaudoin F 2023 Robust sub-kelvin simulations of quantum dot charge sensing *2023 Int. Conf. on Simulation of Semiconductor Processes and Devices (SISPAD)* (IEEE) pp 349–52
[22] Zhang L X, Melnikov D and Leburton J P 2021 Non-monotonic variation of the exchange energy in double elliptic quantum dots *Physical Models for Quantum Dots* (Jenny Stanford Publishing) pp 321–36
[23] Hanson R, Kouwenhoven L P, Petta J R, Tarucha S and Vandersypen L M 2007 *Rev. Mod. Phys.* **79** 1217

[24] Fuhrer A 2003 Phase coherence, orbital and spin states in quantum rings *PhD Thesis* ETH Zurich
[25] Anderson C R, Gyure M F, Quinn S, Pan A, Ross R S and Kiselev A A 2022 *AIP Adv.* **12** 065123
[26] Yadav P, Chakraborty S, Moraru D and Samanta A 2022 *Nanomaterials* **12** 4437
[27] McKinney B and Watson D 2000 *Phys. Rev. B* **61** 4958
[28] Datta S 1997 *Electronic Transport in Mesoscopic Systems* (Cambridge University Press)
[29] Beaudoin F, Philippopoulos P, Zhou C, Kriekouki I, Pioro-Ladrière M, Guo H and Galy P 2022 *Appl. Phys. Lett.* **120** 264001
[30] Van der Wiel W G, De Franceschi S, Elzerman J M, Fujisawa T, Tarucha S and Kouwenhoven L P 2002 *Rev. Mod. Phys.* **75** 1